GEOPHYSICS, VOL. 73, NO. 4 (JULY-AUGUST 2008); P. T51–T61, 10 FIGS., 2 TABLES.
10.1190/1.2939484

An unsplit convolutional perfectly matched layer improved at grazing incidence for seismic wave propagation in poroelastic media

Roland Martin[1], Dimitri Komatitsch[1,2], and Abdelâziz Ezziani[3]

ABSTRACT

The perfectly matched layer (PML) absorbing technique has become popular in numerical modeling in elastic or poroelastic media because of its efficiency in absorbing waves at nongrazing incidence. However, after numerical discretization, at grazing incidence, large spurious oscillations are sent back from the PML into the main domain. The PML then becomes less efficient when sources are located close to the edge of the truncated physical domain under study, for thin slices or for receivers located at a large offset. We develop a PML improved at grazing incidence for the poroelastic wave equation based on an unsplit convolutional formulation of the equation as a first-order system in velocity and stress. We show its efficiency for both nondissipative and dissipative Biot porous models based on a fourth-order staggered finite-difference method used in a thin mesh slice. The results obtained are improved significantly compared with those obtained with the classical PML.

INTRODUCTION

In Komatitsch and Martin (2007), we presented an improved absorbing boundary technique for the purely elastic wave equation based on an unsplit convolutional perfectly matched layer (CPML) and applied it to the seismic wave equation, written as a first-order system in velocity and stress, discretized based on a second-order finite-difference technique in space and time. We showed that this technique is more efficient than the classical perfectly matched layer (PML) at absorbing waves impinging the edges of the model at grazing incidence.

However, real geophysical media often exhibits more complex rheologies, for instance, with mixtures of solids, gases, and liquids. The analysis of elastic waves propagating in fluid-saturated porous media might provide better insight for petrophysical imaging and exploration of natural resources such as hydrocarbon and gas-hydrate reservoirs than single-phase theories represented mainly by elastic or viscoelastic models. The effects of pore pressure, fluid viscosity, porosity, permeability, and slip velocity between phases can be taken into account, and these additional parameters allow the coupling of the propagation of seismic waves and local diffusion of viscous fluids. For instance, numerical modeling of plastic land mines or composite materials consisting of granular solids and pore fluids requires the use of poroelasticlike models (Zeng and Liu, 2001a) because two-phase models are more accurate than purely elastic or viscoelastic models in such a case. Hence, to more realistically model the propagation of waves in heterogeneous media with attenuation caused by fluids, we introduce a CPML for the first-order velocity-stress formulation of the 2D poroelastic wave equation.

Depending on the wavelength at which porous media are studied, different models can be used. The Biot (1956a, 1956b) and Hickey (Hickey and Sabatier, 1997; Quiroga-Goode et al., 2005) models and their variants most commonly are used, although the Hickey model does not dramatically change the amplitude of the waves (Quiroga-Goode et al., 2005). In addition to viscous fluid dissipation, the Hickey model introduces thermomechanical coupling and involves porosity and mass-density perturbations as the porous medium is submitted locally to pressure variations. In spite of all these improvements, some authors consider that the Biot and Hickey theories lead to similar waveforms (Quiroga-Goode et al., 2005). For this reason, we focus on Biot equations in this article.

In terms of numerical simulation of wave propagation, as explained in Komatitsch and Martin (2007), the PML, first introduced for Maxwell's equations by Bérenger (1994), has been developed to efficiently absorb outgoing waves reaching the artificial edges of the computational domain. One of its most attractive properties is that it

Manuscript received by the Editor 18 October 2007; revised manuscript received 18 February 2008; published online 1 July 2008.
[1]Université de Pau et des Pays de l'Adour, Laboratoire de Modélisation et d'Imagerie en Géosciences: CNRS and INRIA Magique-3D, Pau Cedex, France. E-mail: roland.martin@univ-pau.fr; dimitri.komatitsch@univ-pau.fr.
[2]Also at Institut Universitaire de France, Paris, France. E-mail: dimitri.komatitsch@univ-pau.fr.
[3]Université de Pau et des Pays de l'Adour, Laboratoire de Mathématiques Appliquées: CNRS and INRIA Magique-3D, Pau Cedex, France. E-mail: abdelaaziz.ezziani@univ-pau.fr.

has a null reflection coefficient for all angles of incidence and all frequencies before discretization by a numerical scheme. Unfortunately, after discretization, its numerical efficiency is reduced drastically at grazing incidence.

Regarding the numerical simulation of wave propagation in general heterogeneous poroelastic media, the finite-difference method is probably the most widely used technique (e.g., Zhu and McMechan, 1991; Dai et al., 1995; Jianfeng, 1999; Pride et al., 2004; Masson et al., 2006; Sheen et al., 2006; Masson and Pride, 2007). To introduce the classical PML in this method in the case of elastic media, the wave equation usually is formulated as a first-order system in time based on velocity and stress (e.g., Collino and Tsogka, 2001). In the context of poroelastic wave-propagation studies performed based on finite differences, Zeng et al. (2001) applied a split-field formulation of the PML to the Biot system of equations for the displacement formulation, and Zeng and Liu (2001b) applied it to the velocity-stress formulation. Ezziani (2005) developed a split version of the PML applied to the Biot poroelastic equations, based on a more accurate hybrid spectral high-order finite-element technique.

Here we strive to improve the PML for the Biot poroelastic model at grazing incidence, based on an unsplit CPML formulation written in velocity and stress, which also is advantageous in terms of memory storage, and implemented in a fourth-order finite-difference numerical scheme.

Table 1. Physical properties of the heterogeneous two-layer model under study.

Physical variables	Units (IS)	Lower layer	Upper layer
Solid density ρ_s	kg/m^3	2588	2250
Fluid density ρ_f	kg/m^3	952.4	1040
Matrix tortuosity a		2.49	2.42
Porosity ϕ		0.25	0.1
Bulk density $\rho = \varphi\rho_f + (1 - \varphi)\rho_s$	kg/m^3	2179.1	2129
Apparent density $\rho_w = a\rho_f/\varphi$	kg/m^3	9486	25168
α		0.89	0.58
M	Pa	7.71×10^9	7.34×10^9
Damping viscous term K	Ns/m^4	3.38×10^5	3.33×10^6
Fast pressure-wave velocity in the solid V_{Pf}	m/s	2817.33	1921
Slow pressure-wave velocity in the solid V_{Ps}	m/s	740	452.73
Shear-wave velocity in the solid V_S	m/s	1587.4	1072.6
Shear modulus μ	m/s	5.25×10^9	2.4×10^9
Lamé coefficient in solid matrix λ_s	Pa	6.2×10^8	6.0×10^8
Lamé coefficient in saturated medium $\lambda = \lambda_s + M\alpha^2$	Pa	6.7271×10^9	3.069×10^9

THE POROELASTIC WAVE EQUATION: BIOT MODEL AND VELOCITY-STRESS FORMULATION

The differential, or "strong," form of the poroelastic wave equation can be written as (e.g., Carcione, 2007)

$$\begin{aligned}\rho\partial_t^2\mathbf{u}^s + \rho_f\partial_t^2\mathbf{w} &= \nabla\cdot(\mathbf{C}:\nabla\mathbf{u}^s - \alpha P^f I)\\ \rho_f\partial_t^2\mathbf{u}^s + \rho_w\partial_t^2\mathbf{w} &= -\nabla P^f - K\partial_t\mathbf{w}\\ P^f &= -\alpha M\nabla\cdot\mathbf{u}^s - M\nabla\cdot\mathbf{w},\end{aligned}\quad(1)$$

where $\mathbf{u}^s = (u_i^s)_{i=1,D}$ (D denotes the space dimension); $\mathbf{w} = \phi(\mathbf{u}^f - \mathbf{u}^s)$ and $\mathbf{u}^f = (u_i^f)_{i=1,D}$ are, respectively, the solid, relative, and fluid displacement vectors; ϕ is the porosity; and $\mathbf{C}$ is the stiffness tensor of the isotropic elastic solid matrix, defined as

$$\begin{aligned}\sigma_{ij}^s &= (\mathbf{C}:\varepsilon)_{ij} = \lambda_s\delta_{ij}\varepsilon_{kk} + 2\mu\varepsilon_{ij}\\ \varepsilon_{ij} &= \frac{1}{2}\left(\frac{\partial u_i^s}{\partial x_j} + \frac{\partial u_j^s}{\partial x_i}\right),\end{aligned}\quad(2)$$

where indices i and j can be 1 or 2 here in 2D and with the Einstein convention of implicit summation over a repeated index. P^f is the pressure in the fluid. σ^s and ε are, respectively, the stress and strain tensors of the isotropic elastic solid. The stress tensor is $\sigma = \sigma^s - \alpha P^f\mathbf{I}$ of the fluid-filled solid matrix, and $\rho = \phi\rho_f + (1 - \phi)\rho_s$ is the density of the saturated medium, where ρ_s and ρ_f are the solid and fluid densities, respectively, and $\rho_w = a\rho_f/\phi$ with a representing the tortuosity. The shear modulus is μ, and $\lambda_s = \lambda - \alpha^2 M$ is the Lamé coefficient in the solid matrix, where λ is the Lamé coefficient of the saturated matrix. The variable functions of the porosity and bulk moduli of the fluid and solid components of the porous medium are α and M, respectively. The viscous damping coefficient is $K = \kappa/\eta$, where κ is the permeability of the solid matrix and η is the fluid viscosity. All the variables involved in the calculations are given in Table 1.

The frequency-domain form of this equation is

$$\begin{aligned}-\omega^2(\rho\mathbf{u}^s + \rho_f\mathbf{w}) &= \nabla\cdot\sigma\\ -\omega^2(\rho_f\mathbf{u}^s + \rho_w\mathbf{w}) &= -\nabla P^f - i\omega K\mathbf{w}\\ P^f &= -\alpha M\nabla\cdot\mathbf{u}^s - M\nabla\cdot\mathbf{w},\end{aligned}\quad(3)$$

where ω denotes angular frequency and where, for simplicity, we have used the same notation for the different fields in the frequency domain.

In the classical first-order velocity-stress formulation, equations 1 and 2 are rewritten as

$$\begin{aligned}(\rho_w\rho - \rho_f^2)\partial_t\mathbf{v}^s &= \rho_w\nabla\cdot\sigma + \rho_f\nabla P^f + \rho K\mathbf{v}^f\\ (\rho_w\rho - \rho_f^2)\partial_t\mathbf{v}^f &= -\rho_f\nabla\cdot\sigma - \rho\nabla P^f - \rho_f K\mathbf{v}^f\\ \partial_t\sigma &= \mathbf{C}:\nabla\mathbf{v}^s - \alpha\partial_t P^f\mathbf{I}\\ \partial_t P^f &= -\alpha M\nabla\cdot\mathbf{v}^s - M\nabla\cdot\mathbf{v}^f,\end{aligned}\quad(4)$$

where $\mathbf{v}^s = (v_i^s)_{i=1,D}$ and $\mathbf{v}^f = \partial_t\mathbf{w} = (v_i^f)_{i=1,D}$ are the solid and filtration velocity vectors, respectively. As in Zeng and Liu (2001b), we introduce an auxiliary variable ξ and the trace of the strain tensor $\mathrm{Tr}(\varepsilon) = \varepsilon_{ii}$ and rewrite the system as

$$
\begin{aligned}
(\rho_w\rho - \rho_f^2)\partial_t v_i^s &= \rho_w \partial_j \sigma_{ij} + \rho_f \partial_i P^f + \rho_f K v_i^f \\
(\rho_w\rho - \rho_f^2)\partial_t v_i^f &= -\rho_f \partial_j \sigma_{ij} - \rho \partial_i P^f - \rho K v_i^f \\
\partial_t \varepsilon_{ij} &= \frac{1}{2}(\partial_j v_i^s + \partial_i v_j^s) \\
\partial_t \xi &= -\partial_i v_i^f \\
P^f &= -\alpha M \,\mathrm{Tr}(\varepsilon) + M\xi \\
\sigma_{ij}^s &= \lambda_s \delta_{ij} \,\mathrm{Tr}(\varepsilon) + 2\mu\varepsilon_{ij} \\
\sigma_{ij} &= \sigma_{ij}^s - \alpha P^f \delta_{ij}.
\end{aligned} \tag{5}
$$

The frequency-domain form of this system of equations is then

$$
\begin{aligned}
\mathrm{i}\omega(\rho_w\rho - \rho_f^2)v_i^s &= \rho_w \partial_j \sigma_{ij} + \rho_f \partial_i P^f + \rho_f K v_i^f \\
\mathrm{i}\omega(\rho_w\rho - \rho_f^2)v_i^f &= -\rho_f \partial_j \sigma_{ij} - \rho \partial_i P^f - \rho K v_i^f \\
\mathrm{i}\omega\varepsilon_{ij} &= \frac{1}{2}(\partial_j v_i^s + \partial_i v_j^s) \\
\mathrm{i}\omega\xi &= -\partial_i v_i^f \\
P^f &= -\alpha M \,\mathrm{Tr}(\varepsilon) + M\xi \\
\sigma_{ij}^s &= \lambda_s \delta_{ij} \,\mathrm{Tr}(\varepsilon) + 2\mu\varepsilon_{ij} \\
\sigma_{ij} &= \sigma_{ij}^s - \alpha P^f \delta_{ij}.
\end{aligned} \tag{6}
$$

THE CLASSICAL PML FORMULATION IN VELOCITY AND STRESS

The main idea behind the PML technique in 2D lies in reformulating the derivatives in directions x and y in the four layers surrounding the physical domain. In the rest of this article, indices i and j can be replaced by values 1 and 2, which correspond to coordinates x and y, respectively. As in Komatitsch and Martin (2007), a damping profile $d_x(x)$ is defined in the PML region so that $d_x = 0$ inside the main domain and $d_x > 0$ in the PML, and a new complex coordinate $\tilde{x}$ is expressed as

$$
\tilde{x}(x) = x - \frac{\mathrm{i}}{\omega}\int_0^x d_x(s)\mathrm{d}s. \tag{7}
$$

In direction y, a similar damping profile $d_y(y)$ is defined, and a new complex coordinate $\tilde{y}$ is expressed as

$$
\tilde{y}(y) = y - \frac{\mathrm{i}}{\omega}\int_0^y d_y(s)\mathrm{d}s. \tag{8}
$$

Using the fact that

$$
\partial_{\tilde{x}} = \frac{\mathrm{i}\omega}{\mathrm{i}\omega + d_x}\partial_x = \frac{1}{s_x}\partial_x, \tag{9}
$$

with

$$
s_x = \frac{\mathrm{i}\omega + d_x}{\mathrm{i}\omega} = 1 + \frac{d_x}{\mathrm{i}\omega}, \tag{10}
$$

and by retrieving similar expressions of $\partial_{\tilde{y}}$ and s_y, all x derivatives ∂_x are replaced with $\tilde{x}$ derivatives $\partial_{\tilde{x}}$, and y derivatives ∂_y are replaced with $\tilde{y}$ derivatives $\partial_{\tilde{y}}$.

By using the mapping of equation 9, equation 6 is rewritten in terms of x rather than $\tilde{x}$ and y rather than $\tilde{y}$ and then becomes the following (with indices i and j taking the possible values x and y):

$$
\begin{aligned}
\mathrm{i}\omega(\rho_w\rho - \rho_f^2)v_i^s &= \rho_w \frac{1}{s_i}\partial_i \sigma_{ii} + \rho_w \frac{1}{s_j}\partial_j \sigma_{ij} + \rho_f \frac{1}{s_i}\partial_i P^f \\
&\quad + \rho_f K v_i^f, \quad j \neq i \\
\mathrm{i}\omega(\rho_w\rho - \rho_f^2)v_i^f &= -\rho_f \frac{1}{s_i}\partial_i \sigma_{ii} - \rho_f \frac{1}{s_j}\partial_j \sigma_{ij} - \rho \frac{1}{s_i}\partial_i P^f \\
&\quad - \rho K v_i^f, \quad j \neq i \\
\mathrm{i}\omega\varepsilon_{ij} &= \frac{1}{2}\left(\frac{1}{s_j}\partial_j v_i^s + \frac{1}{s_i}\partial_i v_j^s\right) \\
\mathrm{i}\omega\xi &= -\frac{1}{s_1}\partial_1 v_1^f - \frac{1}{s_2}\partial_2 v_2^f \\
P^f &= -\alpha M \,\mathrm{Tr}(\varepsilon) + M\xi \\
\sigma_{ij}^s &= \lambda_s \delta_{ij} \,\mathrm{Tr}(\varepsilon) + 2\mu\varepsilon_{ij} \\
\sigma_{ij} &= \sigma_{ij}^s - \alpha P^f \delta_{ij}.
\end{aligned} \tag{11}
$$

The velocity and strain fields subsequently are split into two components (Zeng and Liu, 2001b), and the result is

$$
\begin{aligned}
\mathrm{i}\omega(\rho_w\rho - \rho_f^2)v_1^{sk} &= \rho_w \frac{1}{s_k}\partial_k \sigma_{1k} + \rho_f \frac{\delta_{1k}}{s_k}\partial_k P^f \\
&\quad + \delta_{2k}\rho_f K v_1^f, \; k = 1,2 \\
\mathrm{i}\omega(\rho_w\rho - \rho_f^2)v_2^{sk} &= \rho_w \frac{1}{s_k}\partial_k \sigma_{k2} \\
&\quad + \delta_{2k}\left(\rho_f \frac{1}{s_k}\partial_k P^f + \rho_f K v_k^f\right), \\
&\quad k = 1,2 \\
\mathrm{i}\omega(\rho_w\rho - \rho_f^2)v_1^{fk} &= -\rho_f \frac{1}{s_k}\partial_k \sigma_{1k} - \rho \frac{\delta_{1k}}{s_k}\partial_k P^f \\
&\quad - \delta_{2k}\rho K v_1^f, \; k = 1,2 \\
\mathrm{i}\omega(\rho_w\rho - \rho_f^2)v_2^{fk} &= -\rho_f \frac{1}{s_k}\partial_k \sigma_{k2} \\
&\quad - \delta_{2k}\left(\rho \frac{1}{s_k}\partial_k P^f + \rho K v_k^f\right), \; k = 1,2 \\
\mathrm{i}\omega\varepsilon_{12}^k &= \frac{1}{2}\left(\frac{\delta_{1k}}{s_1}\partial_1 v_2^s + \frac{\delta_{2k}}{s_2}\partial_2 v_1^s\right), \; k = 1,2 \\
\mathrm{i}\omega\varepsilon_{ii} &= \frac{1}{s_i}\partial_i v_i^s \\
\mathrm{i}\omega\xi^k &= -\frac{1}{s_k}\partial_k v_k^f, \; k = 1,2
\end{aligned}
$$

$$
\begin{aligned}
v_i^s &= v_i^{s1} + v_i^{s2}\\
v_i^f &= v_i^{f1} + v_i^{f2}\\
\varepsilon_{12} &= \varepsilon_{12}^1 + \varepsilon_{12}^2\\
\xi &= \xi^1 + \xi^2,\\
P^f &= -\alpha M\,\mathrm{Tr}(\varepsilon) + M\xi\\
\sigma_{ij}^s &= \lambda_s \delta_{ij}\,\mathrm{Tr}(\varepsilon) + 2\mu\varepsilon_{ij}\\
\sigma_{ij} &= \sigma_{ij}^s - \alpha P^f \delta_{ij}.
\end{aligned}
\tag{12}
$$

Using an inverse Fourier transform, we return to the time domain and obtain the final classical PML formulation of the poroelastic equations in a split form:

$$
\begin{aligned}
&(\partial_t + d_k)(\rho_w\rho - \rho_f^2)v_1^{sk}\\
&\quad = \rho_w\partial_k\sigma_{1k} + \delta_{1k}\rho_f\partial_k P^f + \delta_{2k}\rho_f K\\
&\qquad \times\left(v_1^f + d_k\int_{-\infty}^{t} v_1^f d\tau\right),\ k = 1,2
\end{aligned}
$$

$$
\begin{aligned}
&(\partial_t + d_k)(\rho_w\rho - \rho_f^2)v_2^{sk}\\
&\quad = \rho_w\partial_k\sigma_{k2} + \delta_{2k}\\
&\qquad \times\left(\rho_f\partial_k P^f + \rho_f K\left(v_2^f + d_k\int_{-\infty}^{t} v_2^f d\tau\right)\right),\ k = 1,2
\end{aligned}
$$

$$
\begin{aligned}
&(\partial_t + d_k)(\rho_w\rho - \rho_f^2)v_1^{fk}\\
&\quad = -\rho_f\partial_k\sigma_{1k} - \delta_{1k}\rho\partial_k P^f - \delta_{2k}\rho K\\
&\qquad \times\left(v_1^f + d_k\int_{-\infty}^{t} v_1^f d\tau\right),\ k = 1,2
\end{aligned}
$$

$$
\begin{aligned}
&(\partial_t + d_k)(\rho_w\rho - \rho_f^2)v_2^{fk}\\
&\quad = -\rho_f\partial_k\sigma_{k2} - \delta_{2k}\\
&\qquad \times\left(\rho\partial_k P^f + \rho K\left(v_2^f + d_k\int_{-\infty}^{t} v_2^f d\tau\right)\right),\ k = 1,2
\end{aligned}
$$

$$
(\partial_t + d_k)\varepsilon_{12}^k = \frac{1}{2}(\delta_{1k}\partial_1 v_2^s + \delta_{2k}\partial_2 v_1^s),\ k = 1,2
$$

$$
(\partial_t + d_i)\varepsilon_{ii} = \partial_i v_i^s
$$

$$
(\partial_t + d_k)\xi^k = -\partial_k v_k^f,\ k = 1,2
$$

$$
\begin{aligned}
v_i^s &= v_i^{s1} + v_i^{s2}\\
v_i^f &= v_i^{f1} + v_i^{f2}\\
\varepsilon_{12} &= \varepsilon_{12}^1 + \varepsilon_{12}^2\\
\xi &= \xi^1 + \xi^2,\\
P^f &= -\alpha M\,\mathrm{Tr}(\varepsilon) + M\xi\\
\sigma_{ij}^s &= \lambda_s\delta_{ij}\,\mathrm{Tr}(\varepsilon) + 2\mu\varepsilon_{ij}\\
\sigma_{ij} &= \sigma_{ij}^s - \alpha P^f\delta_{ij}.
\end{aligned}
\tag{13}
$$

The dissipative integral term that appears on the right-hand side of the equations is computed by introducing an auxiliary memory variable defined as

$$
\mathbf{B}(x,y,t) = \int_{-\infty}^{t} \mathbf{v}^f d\tau\,, \tag{14}
$$

which adds another equation to system 13 (Zeng and Liu, 2001b):

$$
\partial_t\mathbf{B}(x,y,t) = \mathbf{v}^f. \tag{15}
$$

Unfortunately, as we show in the section about numerical tests below, this classical PML formulation does not give satisfactory results at grazing incidence. Therefore, we introduce an unsplit CPML technique improved at grazing incidence for poroelastic media.

A CPML TECHNIQUE IMPROVED AT GRAZING INCIDENCE FOR THE BIOT POROELASTIC EQUATIONS

In this section, the CPML technique developed in the purely elastic case in Komatitsch and Martin (2007) is used for the first-order formulation of the poroelastic wave equation. The key idea of the CPML (Roden and Gedney, 2000) lies in finding a more general choice for s_x than that of equation 9 by introducing a real variable $\alpha_x \geq 0$ so that

$$
s_x = 1 + \frac{d_x}{\alpha_x + \mathrm{i}\omega}. \tag{16}
$$

Using some simple algebraic operations and making use of the recursive convolution method of Luebbers and Hunsberger (1992), we demonstrated in Komatitsch and Martin (2007) that this generalized choice can be implemented in practice by introducing a memory variable ψ_x updated at each time step according to

$$
\psi_x^n = b_x\psi_x^{n-1} + a_x(\partial_x)^{n-1/2}, \tag{17}
$$

where:

$$
b_x = e^{-(d_x+\alpha_x)\Delta t} \quad \text{and} \quad a_x = \frac{d_x}{d_x + \alpha_x}(b_x - 1), \tag{18}
$$

and that then, in the elastic case, the unsplit CPML formulation can be implemented easily in a finite-difference code without PML by simply replacing the spatial derivatives ∂_x with $\partial_x + \psi_x$ and advancing ψ_x in time using the same time-evolution scheme as for the other (existing) variables.

This same idea can be used to define a CPML formulation for the poroelastic wave equation by introducing such a memory variable for each spatial derivative that appears in equation 5. In terms of numerical efficiency, the memory storage needed to implement CPML for poroelastic equations is similar to the second-order velocity-stress formulation of Zeng and Liu (2001b), as can be seen in Table 2. Furthermore, the classical PML requires an extra memory variable to handle the dissipative term that is not present in the CPML formulation, the CPML being essentially based on the com-

plex change of variable for first-derivative calculations independently of the presence or absence of dissipative terms.

A convenient property shared by the classical PML and the CPML is that the same method can be used to define a PML along the y-axis and that in the corners, the different memory variables simply are summed (i.e., the corners are handled automatically by the formulation).

NUMERICAL TESTS

To validate the new CPML model, we use a spatial discretization of the equations based on a classical staggered-grid fourth order in space and second order in time, similar to that used, for example, by Levander (1988), Graves (1996), and Moczo et al. (2000) in the elastic case and by Pride et al. (2004) and Masson et al. (2006) in the Biot poroelastic case. We use a fourth-order discretization scheme in space to increase accuracy and to enable us to use grids of reasonable size for sources of relatively high-frequency content, and we use a second-order leapfrog scheme for the integration in time (e.g., Virieux, 1986). The eight variables v_x, v_y, σ_{xx}, σ_{yy}, σ_{xy}, v_x^f, v_y^f, and P^f, as well as the memory variables that implement the recursive convolution, are discretized on the grid represented in Figure 1.

Nondissipative heterogeneous media

To study the behavior of the CPML in a heterogeneous nondissipative medium in the case of waves propagating at grazing incidence, we consider a first experiment in which we simulate the propagation of poroelastic waves in a heterogeneous medium 70 m $\times$ 310 m in size, surrounded by four PML layers of 10 grid points each. The medium comprises two horizontal layers whose physical properties are the same as that described by Zeng and Liu (2001b) and shown in Table 1. The interface between the two layers is located at $y = 105$ m. To discretize the equations in space, the spatial step must be selected according to the size of solid pores and grains. Indeed, in a poroelastic model, fast pressure (P) and shear (S) waves mainly resolve macroscopic geologic structures of a few tens or hundreds of meters throughout the seismic frequency range (typically 1 Hz through 100 Hz), whereas slow P- and S-waves are related to the microscopic scale.

The system of differential equations derives from homogenization considerations, and the wavelengths must be larger than a typical averaging elementary volume, which in turn must be at least 10 times larger than the pore or grain sizes (Pride et al., 2004). Numerically, this is very important and must be kept in mind because some nonphysical waves and unwanted numerical instabilities or numerical dispersion can appear in the simulations. In the following, all these considerations are taken into account. The spatial discretization step is the same in both directions and is equal to $\Delta x = \Delta y = 0.5$ m, i.e., the grid (including the PML layers) has a total size of 141×621 grid points.

Masson et al. (2006) have analyzed the stability of the scheme and have shown that one must ensure the necessary but not sufficient stability condition $\rho\rho_w - \rho_f^2 > 0$. The general stability criterion is a nonlinear inf-sup condition, which is difficult to use in practice. However, for the typical values of the parameters used in our study, the stability condition is similar to the classical Courant condition of the elastic case. In particular, if ρ_w/ρ_f is large (here approximately 9.96 in the bottom layer and 24.2 in the top layer), the Courant number of the discretized poroelastic system of equations can be extrapolated from the elastic case in one, two, or three dimensions, and the time step Δt must obey the Courant-Friedrichs-Lewy (Courant et al., 1928) stability condition

$$\frac{c_p \Delta t}{\Delta x} \leq \frac{1}{(c_1 + c_2)\sqrt{D}} \tag{19}$$

in the case of a uniform mesh in all spatial directions, where D is the spatial dimension of the problem, where $c_1 = 9/8$ and $c_2 = 1/24$ for the fourth-order spatial discretization scheme used, and $c_1 = 1$ and $c_2 = 0$ for the second-order scheme.

It can be observed that the Courant condition for the fourth-order scheme is slightly lower than that for the second-order scheme, by a factor $6/7 = 0.857$, but this is balanced by the fact that a larger spatial step and therefore a smaller number of grid points can be used, which reduces the total number of calculations and the amount of memory storage. We select a time step $\Delta t = 0.1$ ms, i.e., a ratio of 0.562 in the stability condition 19, slightly below the upper limit of $1/\sqrt{2} \times 0.857 \simeq 0.601$. The simulation is performed for 100,000 time

Table 2. The maximum number of arrays needed in the PML layers to implement the method in two dimensions.[a]

	No PML	PML without total	PML with total	CPML
2D	8	16	24	19

[a]"PML without total" is the classical PML technique (see, e.g., Zeng and Liu, 2001b) without storing the total field, i.e., the sum of the split components, which then is recomputed in each loop. "PML with total" is the classical PML technique, storing the total field. "CPML" is the CPML technique. This maximum number is reached in regions in which all the PML layers are present, i.e., in the corners of the domain. The small difference in storage applies only in the PML layers and not in the main domain and is therefore negligible. For comparison, we also recall the number of arrays needed when no absorbing conditions are implemented in the finite-difference technique.

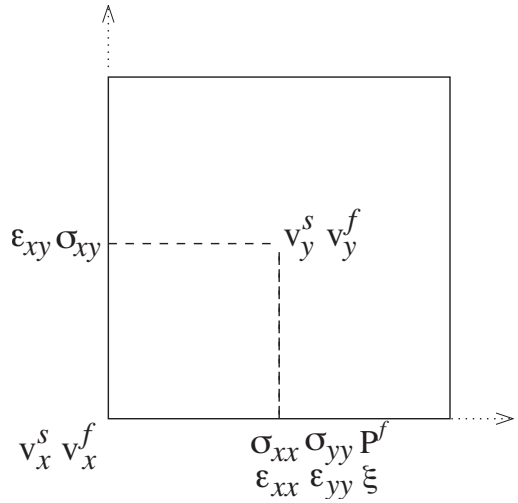

Figure 1. Two-dimensional staggered spatial finite-difference grid of Madariaga (1976) used classically to discretize the equations of elastodynamics. In our study, the staggered grid is applied to the velocity-stress formulation of the Biot poroelastic wave equation, as in Zeng and Liu (2001b) and Masson et al. (2006). The positions of discrete stresses, fluid pressure, strains, and velocity components in the solid matrix and in the fluid are indicated.

steps, i.e., for a total duration of 10 s. A pressure point source is located close to the left PML layer at 10 grid points from its base (x_s = 55 m, y_s = 150 m). The source is the first derivative of a Gaussian in time, with a central frequency f_0 = 40 Hz, shifted in time by t_0 = 0.03 s so that it will have null initial conditions.

PML layers are implemented on the four edges of the grid. As in Gedney (1998) and Collino and Tsogka (2001), the damping profile in the PML is chosen as $d_x(x) = d_0(x/L)^N$ along the x-axis and $d_y(y) = d_0(y/L)^N$ along the y-axis, where L is the thickness of the absorbing layer, $N = 2$, and $d_0 = -(N+1)V_P^{\max}\log(R_c)/2L \simeq 5827.86$, $V_P^{\max}$ being equal to the speed of the fast pressure wave and R_c being the target theoretical reflection coefficient, chosen here as 0.1%. As in Roden and Gedney (2000), we make α_x and α_y vary linearly in the PML layer between a maximum value $\alpha_{\max}$ at the beginning of the PML and zero at the top. As in Festa and Vilotte (2005), we then take $\alpha_{\max} = \pi f_0$, where f_0 is the central frequency of the source defined above.

On the external edges of the grid, i.e., at the top of each PML, we impose a Dirichlet condition on the velocity vector ($\mathbf{v} = \mathbf{0}$ for all t). Because of the aspect ratio of the grid, the waves reach the PML layers at grazing incidence in several areas of the mesh. The fast pressure waves, the shear waves, and the slow pressure waves are absorbed gradually in the PMLs. Snapshots of the simulation (Figure 2) do not exhibit significant spurious oscillations in the case of the CPML condition, whereas nonphysical spurious oscillations arise in the case of the classical PML (Figure 3).

The vertical component of the velocity in the solid phase is recorded at two receivers located close to the edges of the grid, at

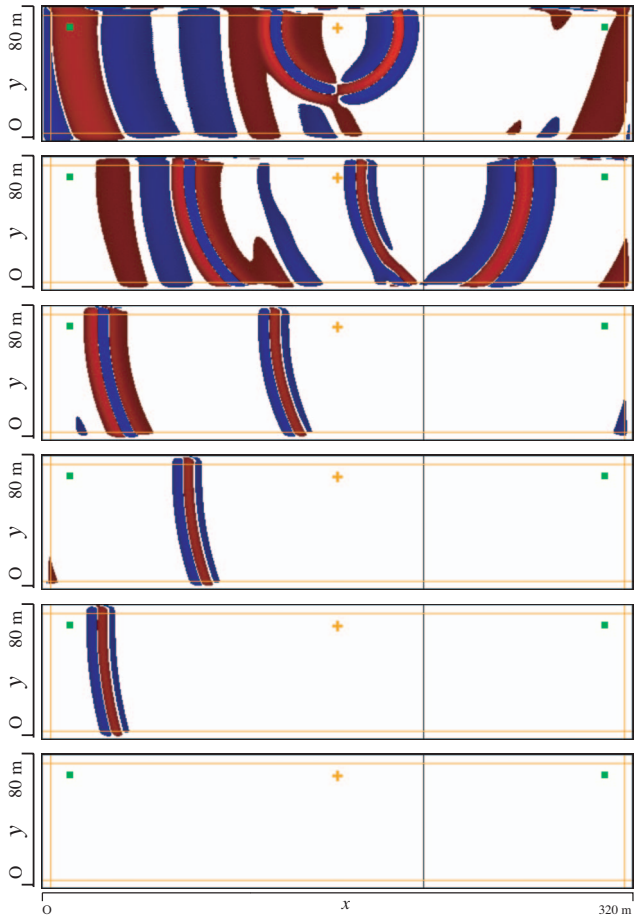

Figure 2. Snapshots of the v_y^s component of the 2D velocity vector in the solid matrix for a nondissipative porous model corresponding to a thin slice with CPML conditions implemented on the four sides, at time 0.1 s (top), 0.2 s, 0.4 s, 0.5 s, and 0.6 s (bottom). This is shown in red (positive) or blue (negative) when it has an amplitude higher than a threshold of 1% of the maximum, and the normalized value is raised to the power 0.3 to enhance small amplitudes that otherwise would not be clearly visible. The orange cross indicates the location of the source and the green squares the position of receivers at which seismograms represented in the left column of Figure 4 are recorded. The four vertical or horizontal orange lines represent the edge of each PML layer. The interface between the two media is represented by a black line. No spurious wave of significant amplitude is visible, even at grazing incidence. The snapshots have been rotated 90° left to fit on the page.

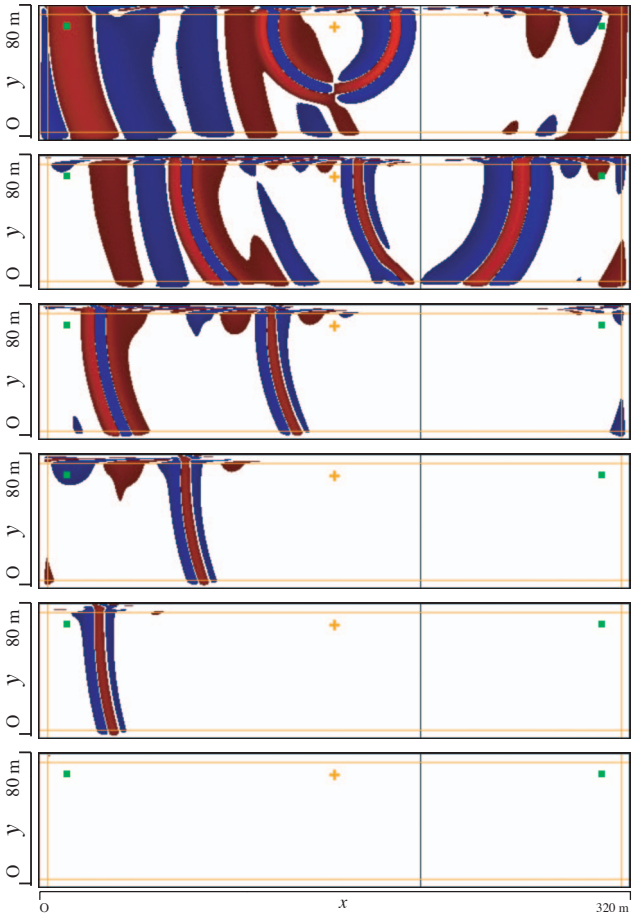

Figure 3. Snapshots of the v_y^s component of the 2D velocity vector in the solid matrix for a nondissipative porous model corresponding to a thin slice with classical PML conditions (Zeng and Liu, 2001b) implemented on the four sides, at time 0.1 s (top), 0.2 s, 0.4 s, 0.5 s, and 0.6 s (bottom). This is shown in red (positive) or blue (negative) when it has an amplitude higher than a threshold of 1% of the maximum, and the normalized value is raised to the power 0.3 to enhance small amplitudes that would otherwise not be clearly visible. The orange cross indicates the location of the source and the green squares the position of receivers at which seismograms represented in the right column of Figure 4 are recorded. The four vertical or horizontal orange lines represent the edge of each PML layer. The interface between the two media is represented by a black line. Compared with Figure 2, spurious waves appear at grazing incidence along the edges of the model and send spurious energy back into the main domain. The snapshots have been rotated 90° left to fit on the page.

the bottom and top of the slice in the lower and upper right corners, 10 grid points above the lower PML and 10 grid points below the upper PML in ($x_1 = 55$ m, $y_1 = 10$ m) and ($x_2 = 55$ m, $y_2 = 290$ m) to analyze the effects of the boundary conditions. In Figure 4, solutions with CPML and with the classical PML for the vertical component of the velocity vector in the solid matrix are compared with the analytical solution of Diaz and Ezziani (J. Diaz and A. Ezziani, personal communication, 2008) derived from the analytical solution for a single layer (Dai et al., 1995; Ezziani, 2005, 2006). The residual error is small in the case of CPML, whereas the solution with the classical PML is distorted significantly.

We now study the decay of energy in the mesh to analyze more precisely the efficiency of the CPML at grazing incidence. Figure 5 shows the decay in time of the total energy E

$$E = \frac{1}{2}\rho\|\mathbf{v}^s\|^2 + \frac{1}{2}\sum_{i=1}^{D}\sum_{j=1}^{D}\sigma_{ij}^s\varepsilon_{ij} + \frac{1}{2}\rho_w\|\mathbf{v}^f\|^2 + \frac{1}{2M}P^{f^2} + \rho_f\mathbf{v}^s\cdot\mathbf{v}^f \tag{20}$$

in the inner part of the model (i.e., in the medium without the four PML layers) for the simulation presented in Figure 2. In Figure 5, we compare the evolution of total energy over 10,000 steps with CPML to that calculated with the classical PML. Between approximately 0 s and 0.1 s, the source injects energy into the system. Then the energy transported by the different P- and S-waves gradually is absorbed by the PML layers, and after approximately 0.6 s all converted and transmitted waves should have disappeared and no energy should remain in the medium. All the remaining energy is therefore spurious.

At 0.65 s, a total energy of 7.03×10^{-4} J remains in the case of PML, and a total energy of 3.38×10^{-6} J remains in the case of CPML (i.e., smaller by a factor of 208). It is also interesting to study the issue of the stability of the CPML for longer time periods. It is known that in numerous PML models (e.g., Maxwell's equations), weak or strong instabilities can develop for long simulations (e.g., Abarbanel et al., 2002; Bécache and Joly, 2002; Bécache et al., 2004). To analyze long-time stability from a numerical point of view, we show in Figure 5 the evolution of total energy over 10 s (i.e., 100,000 time steps) for the experiments of Figures 2 and 3. It decreases continuously, and no instabilities are observed on this semilogarithmic curve, which means that the discrete CPML is stable up to 100,000 steps.

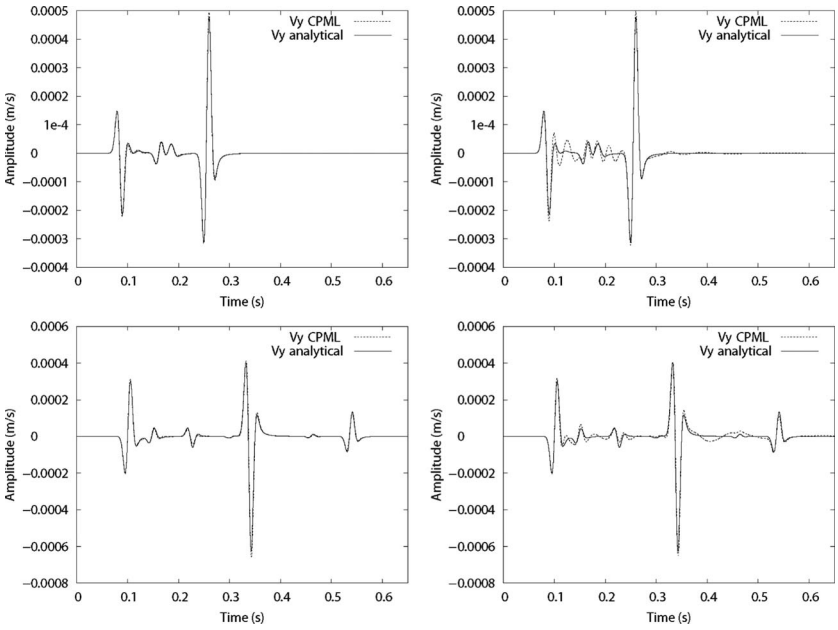

Figure 4. (Left column): Time evolution of the numerical solution with CPML (dotted line) for the v_y^s component of the velocity vector in the solid matrix at the first receiver in ($x = 55$ m, $y = 10$ m) (top) and second receiver in ($x = 55$ m, $y = 290$ m) (bottom) compared with the analytical solution of Diaz and Ezziani (J. Diaz and A. Ezziani, personal communication, 2008; solid line) for the numerical experiment of Figure 2. At these two receivers located close to the PML layer and far from the source (at both ends of the slice 10 grid points away from the beginning of the PML layer), the agreement is good in spite of the grazing incidence. This illustrates the good efficiency of the CPML. (Right column): Same comparison when the classical PML of Zeng and Liu (2001b) is used in the numerical experiment of Figure 3. Large spurious oscillations appear, and the fast P-wave and S-wave are distorted significantly. The other waves (transmitted and converted on the discontinuity) are not computed correctly.

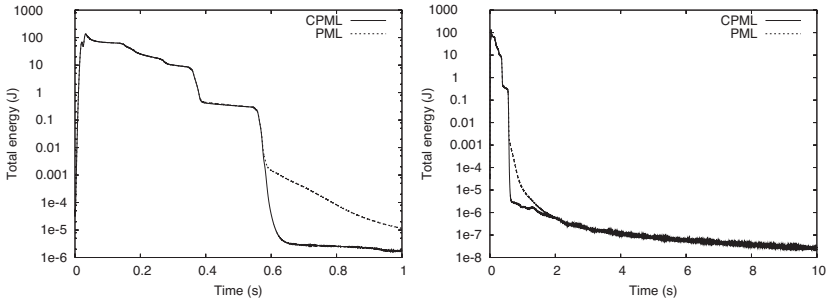

Figure 5. Left: Decay of total energy with time in the main domain (without the four PML layers) on a semilogarithmic scale for the simulations presented in Figures 2 and 3. The solid and dashed lines correspond, respectively, to the CPML and PML cases. Between approximately 0 s and 0.1 s, energy is injected by the source in the medium. Then the energy carried by the P- and S-waves is absorbed gradually in the PML layers. The slow P-wave and the different waves converted and transmitted at the model discontinuity are absorbed in turn, which results in a steep decay of total energy. After approximately 0.6 s, theoretically no energy should remain in the medium because all waves have left the domain. Hence, all the remaining energy is spurious and constitutes a good test of the efficiency of the absorbing conditions. In the case of PML, at 0.65 s, a total energy around 7.03×10^{-4} J remains, whereas a total energy of 3.38×10^{-6} J is present in the case of CPML, i.e., a factor of 208 smaller. Right: To study the stability of CPML at longer times, we make the experiment of Figure 2 last for 100,000 time steps (i.e., 10 s). Total energy decreases continuously, and no instabilities are observed on this semilogarithmic curve, which means that the discrete CPML is stable up to 100,000 steps.

DISSIPATIVE HETEROGENEOUS CASE

In the case of a dissipative heterogeneous medium, we study the behavior of the CPML at grazing incidence for the same thin heterogeneous slice, but with a higher central frequency $f_0 = 80$ Hz shifted in time by $t_0 = 0.015$ s and with a nonzero viscous term K (given in Table 1). In the presence of dissipation, the slow waves are not present. Because the slow wave velocities given in Table 1 are smaller than the S-wave velocity by a factor of almost two, we therefore can reasonably use the same mesh size and grid spacing as in the nondissipative case, although the frequency is twice as high.

We do not have an analytical solution in the dissipative case, therefore we compare the CPML and the PML of Zeng and Liu (2001b) with a numerical reference solution obtained with the hybrid spectral high-order finite-element method (MFEMSPEC) of Ezziani (2005), used on a very large mesh to mimic an infinite domain. In Figure 6, the CPML solution does not exhibit significant spurious oscillations. However, in Figure 7, in the case of the classical PML, oscillations appear at grazing incidence, similar to the nondissipative case above.

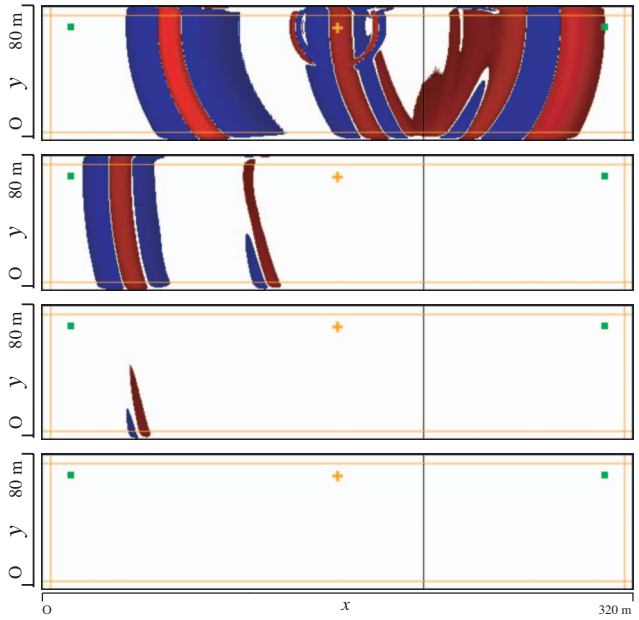

Figure 6. Snapshots of the v_y^s component of the 2D velocity vector in the dissipative case for a model corresponding to a thin slice with CPML conditions implemented on the four sides, at time 0.06 s (top), 0.12 s, 0.18 s, and 0.24 s (bottom). This is shown in red (positive) or blue (negative) when it has an amplitude higher than a threshold of 1% of the maximum, and the normalized value is raised to the power 0.3 to enhance small amplitudes that otherwise would not be represented clearly. The central frequency has been increased to 80 Hz, compared with the 40 Hz used in Figure 2 to reduce the large wavelengths caused by viscous smoothing. The orange cross indicates the location of the source and the green squares the position of receivers at which seismograms represented in Figures 8 and 9 are recorded. The four vertical or horizontal orange lines represent the edge of each PML layer. The interface between the two media is represented by a black line. In this case, waves are smoothed, and the slow waves are filtered by viscous damping. No spurious wave of significant amplitude is visible, even at grazing incidence. The snapshots have been rotated 90° left to fit on the page.

To study more precisely the difference with the MFEMSPEC reference solution, in particular close to the boundary and at a long distance from the source, Figures 8 and 9 compare the vertical component of the velocity vector in the solid matrix and the fluid pressure computed with CPML or with the classical PML to the reference solution. Large discrepancies can be observed in the case of the classical PML caused by the generation of growing oscillations inside and along the PML, whereas much smaller discrepancies are present in the case of CPML.

In the viscous dissipative case, the energy as expected is damped much faster than in the nondissipative case (Figure 10). Viscous damping and PML absorption seem to compete in a similar proportion. Energy decays faster in the case of CPML than in the case of PML and reaches 4.48×10^{-9} J at 2 s for CPML, whereas 1.15×10^{-7} J remains in the case of PML, i.e., a factor of 26 times larger. Again, we observe that in the case of PML, total energy decreases slower than with CPML after 0.25 s because of the generation of spurious oscillations in the PML layer, which develop along the layer and send spurious energy back into the domain. All spurious waves then are absorbed gradually by the upper and lower PML lay-

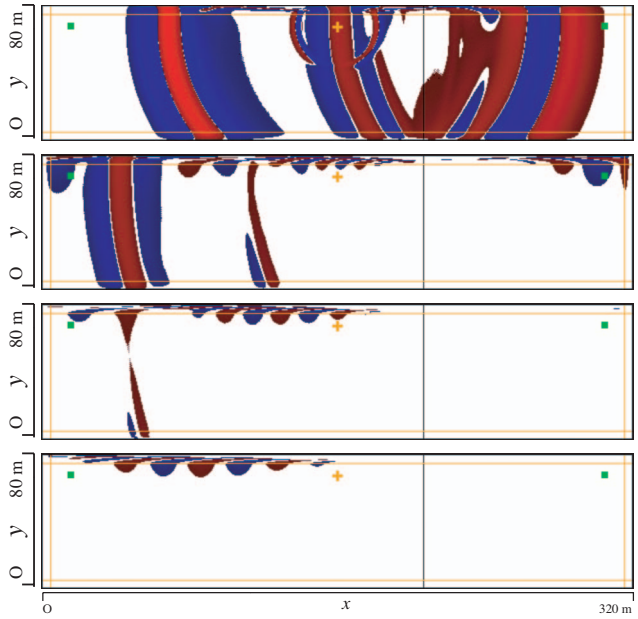

Figure 7. Snapshots of the v_y^s component of the 2D velocity vector in the dissipative case for a model corresponding to a thin slice with classical PML conditions of Zeng and Liu (2001b) implemented on the four sides, at time 0.06 s (top), 0.12 s, 0.18 s, and 0.24 s (bottom). This is shown in red (positive) or blue (negative) when it has an amplitude higher than a threshold of 1% of the maximum, and the normalized value is raised to the power 0.3 to enhance small amplitudes that otherwise would not be represented clearly. The central frequency has been increased to 80 Hz compared with the 40 Hz used in Figure 3 to reduce the large wavelengths caused by viscous smoothing. The orange cross indicates the location of the source and the green squares the position of receivers at which seismograms represented in Figures 8 and 9 are recorded. The four vertical or horizontal orange lines represent the edge of each PML layer. The interface between the two media is represented by a black line. In this case, waves are smoothed, and the slow waves are filtered by viscous damping. Compared with Figure 6, spurious waves appear at grazing incidence along the edges of the model and send spurious energy back into the main domain. The snapshots have been rotated 90° left to fit on the page.

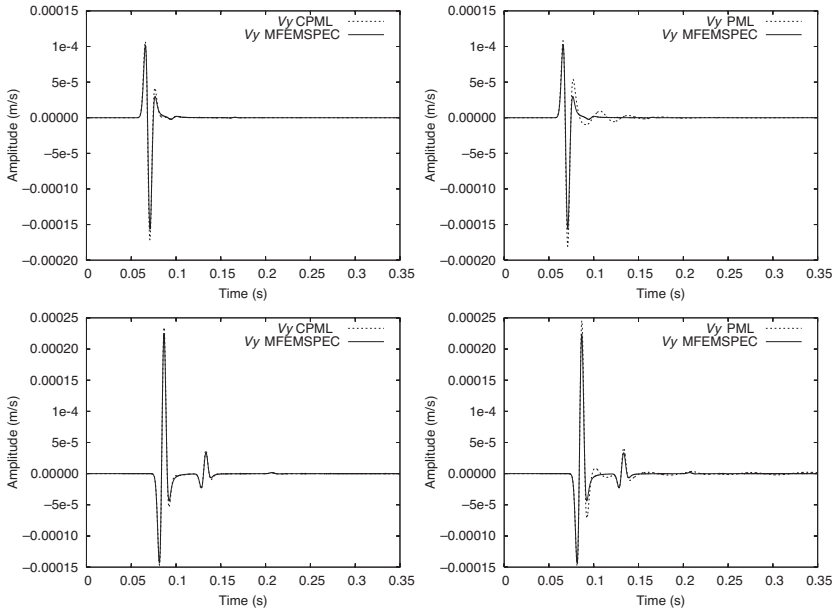

Figure 8. Top: Seismograms of the v_y^s component of the velocity vector in the solid matrix at the first receiver in ($x = 55$ m, $y = 10$ m), i.e., 10 grid points away from the beginning of the absorbing layers in the case of CPML (left, dotted line) and of the classical PML (right, dotted line) compared with a reference solution (solid line) computed using the high-order finite-element method of Ezziani (2006) on a very large domain which mimics an infinite medium. The agreement obtained in the case of CPML is good and no significant spurious waves are recorded, whereas in the case of the classical PML, large spurious oscillations are present. The reference solution is numerical and therefore some of the discrepancies could come from small numerical dispersion in that reference solution. However, that reference solution does not contain any artefact coming back from the edges of the grid because it is computed purposely on a very large grid that mimics an infinite medium.

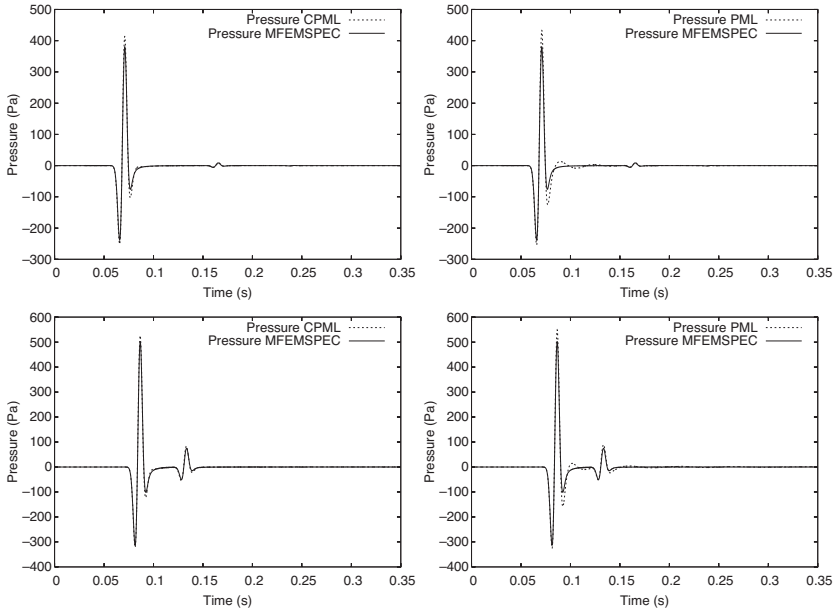

Figure 9. Same figure as Figure 8 but for the fluid pressure P^f. The conclusions regarding the improved efficiency of CPML compared with PML remain the same.

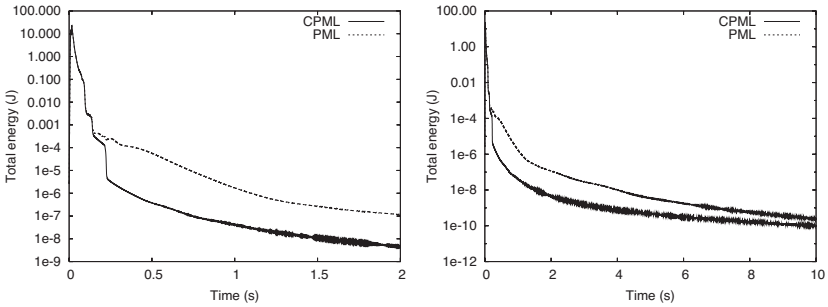

Figure 10. Left: Decay of total energy with time in the main domain (without the four PML layers) on a semilogarithmic scale for the simulations presented in Figures 6 and 7. Between approximately 0 s and 0.1 s, energy is injected by the source in the medium. Then the energy carried by the P- and S-waves is absorbed gradually in the PML layers. The different waves converted and transmitted at the model discontinuity are then absorbed, which results in a steep decay of total energy. After approximately 0.3 s, theoretically no energy should remain in the medium because all waves have left the domain, and all the remaining energy is therefore spurious. This constitutes a good test of the efficiency of the absorbing conditions. One can observe that energy in the case of the classical PML decreases slower than in the case of CPML because of spurious energy sent back in the main domain at grazing incidence. At 2 s, a total energy of 1.15×10^{-7} J remains in the case of PML, whereas a total energy of 4.48×10^{-9} J remains in the case of CPML, i.e., a factor of 26 smaller. Right: To study the stability of CPML at longer times in the dissipative case, we make the experiment of Figures 6 and 7 last for 100,000 time steps (i.e., 10 s) instead of 10,000. Total energy decreases continuously, and no instabilities are observed on this semilogarithmic curve, which means that the discrete CPML is stable up to 100,000 steps. One can notice tiny oscillations because total energy is so small that we start to see the effect of roundoff of floating-point numbers of the computer.

ers, making the total energy decrease toward small values that nonetheless remain higher by several orders of magnitude than with CPML after a long time. Again, the CPML solution is stable for long times, up to a total duration of 10 s (i.e., 100,000 time steps).

CONCLUSIONS

In a previous article, we improved the classical perfectly matched layer technique at grazing incidence for elastic media based on an unsplit convolutional technique called CPML. Here, we applied the CPML to Biot poroelastic media at a cost that is similar in terms of memory storage to that of the classical PML. To demonstrate its improved behavior, we compared both CPML and classical PML implemented in a fourth-order staggered finite-difference scheme in space in a thin slice to the analytical solution in the nondissipative case and to a hybrid spectral/finite-element method in the dissipative case. The study of the decay of total energy in the medium without the PML layers confirmed that CPML is more efficient than PML at grazing incidence and showed that CPML remains stable for simulations at long times.

The source code of our finite-difference program SEISMIC _CPML is freely available under CeCILL license (a French equivalent of GNU GPL) from www.univ-pau.fr/~dkomati1.

ACKNOWLEDGMENTS

The authors would like to thank Stephen D. Gedney for fruitful discussions and for providing them with his CPML software package for Maxwell's equations and Julien Diaz for providing them with the analytical solution for the first validation test. The comments and suggestions of two anonymous reviewers and of the associate editor, assistant editor Vladimir Grechka, and editor Kees Wapenaar helped to improve the manuscript. This material is based in part on research supported by European FP6 Marie Curie International Reintegration Grant MIRG-CT-2005-017461.

REFERENCES

Abarbanel, S., D. Gottlieb, and J. S. Hesthaven, 2002, Long time behavior of the perfectly matched layer equations in computational electromagnetics: Journal of Scientific Computing, **17**, 405–422.

Bécache, E., and P. Joly, 2002, On the analysis of Bérenger's perfectly matched layers for Maxwell's equations: Mathematical Modelling and Numerical Analysis, **36**, 87–120.

Bécache, E., P. G. Petropoulos, and S. G. Gedney, 2004, On the long-time behavior of unsplit perfectly matched layers: IEEE Transactions on Antennas and Propagation, **52**, 1335–1342.

Bérenger, J. P., 1994, A perfectly matched layer for the absorption of electromagnetic waves: Journal of Computational Physics, **114**, 185–200.

Biot, M. A., 1956a, Theory of propagation of elastic waves in a fluid-saturated porous solid. I: Low-frequency range: Journal of the Acoustical Society of America, **28**, 168–178.

———, 1956b, Theory of propagation of elastic waves in a fluid-saturated porous solid. II: Higher-frequency range: Journal of the Acoustical Society of America, **28**, 179–191.

Carcione, J. M., 2007, Wave fields in real media: Wave propagation in anisotropic, anelastic, porous, and electromagnetic media, 2nd ed.: Elsevier Science.

Collino, F., and C. Tsogka, 2001, Application of the PML absorbing layer model to the linear elastodynamic problem in anisotropic heterogeneous media: Geophysics, **66**, 294–307.

Courant, R., K. O. Friedrichs, and H. Lewy, 1928, Über die partiellen Differenzengleichungen der mathematischen Physik: Mathematische Annalen, 100, 32–74.

Dai, N., A. Vafidis, and E. R. Kanasevich, 1995, Wave propagation in heterogeneous, porous media: A velocity-stress, finite-difference method: Geophysics, **60**, 327–340.

Ezziani, A., 2005, Modélisation mathématique et numérique de la propagation d'ondes dans des milieux viscoélastiques et poroélastiques: Ph.D. thesis, Université Paris IX, France.

———, 2006, Ondes dans les milieux poroélastiques: Analyse du modèle de Biot: Revue Africaine de la Recherche en Informatique et Mathématiques Appliquées ARIMA, 5, 95–109.

Festa, G., and J. P. Vilotte, 2005, The Newmark scheme as velocity-stress time-staggering: An efficient PML implementation for spectral-element simulations of elastodynamics: Geophysical Journal International, **161**, 789–812.

Gedney, S. D., 1998, The perfectly matched layer absorbing medium, *in* A. Taflove, ed., Advances in computational electrodynamics: The finite-difference time-domain method: Artech House, 263–343.

Graves, R. W., 1996, Simulating seismic wave propagation in 3D elastic media using staggered-grid finite differences: Bulletin of the Seismological Society of America, **86**, 1091–1106.

Hickey, C. J., and J. M. Sabatier, 1997, Choosing Biot parameters for modeling water-saturated sand: Journal of the Acoustical Society of America, **102**, 1480–1484.

Jianfeng, Z., 1999, Quadrangle-grid velocity-stress finite-difference method for poroelastic wave equations: Geophysical Journal International, **139**, 171–182.

Komatitsch, D., and R. Martin, 2007, An unsplit convolutional perfectly matched layer improved at grazing incidence for the seismic wave equation: Geophysics, **72**, no. 5, SM155–SM167.

Levander, A. R., 1988, Fourth-order finite-difference P-SV seismograms: Geophysics, **53**, 1425–1436.

Luebbers, R. J., and F. Hunsberger, 1992, FDTD for Nth-order dispersive media: IEEE Transactions on Antennas and Propagation, **40**, 1297–1301.

Madariaga, R., 1976, Dynamics of an expanding circular fault: Bulletin of the Seismological Society of America, **66**, 639–666.

Masson, Y. J., and S. R. Pride, 2007, Poroelastic finite-difference modeling of seismic attenuation and dispersion due to mesoscopic-scale heterogeneity: Journal of Geophysical Research, **112**, B03204.

Masson, Y. J., S. R. Pride, and K. T. Nihei, 2006, Finite-difference modeling of Biot's poroelastic equations at seismic frequencies: Journal of Geophysical Research, **111**, B10305.

Moczo, P., J. Kristek, and L. Halada, 2000, 3D fourth-order staggered-grid finite-difference schemes: Stability and grid dispersion: Bulletin of the Seismological Society of America, **90**, 587–603.

Pride, S. R., J. G. Berryman, and J. M. Harris, 2004, Seismic attenuation due to wave-induced flow: Journal of Geophysical Research, **109**, 681–693.

Quiroga-Goode, G., S. Jiménez-Hernández, M. A. Pérez-Flores, and R. Padilla-Hernández, 2005, Computational study of seismic waves in homogeneous dynamic-porosity media with thermal and fluid relaxation: Gauging Biot theory: Journal of Geophysical Research, **110**, B07303.

Roden, J. A., and S. D. Gedney, 2000, Convolution PML (CPML): An efficient FDTD implementation of the CFS-PML for arbitrary media: Microwave and Optical Technology Letters, **27**, 334–339.

Sheen, D.-H., K. Tuncay, C.-E. Baag, and P. J. Ortoleva, 2006, Parallel implementation of a velocity-stress staggered-grid finite-difference method for 2D poroelastic wave propagation: Computers and Geosciences, **32**, 1182–1191.

Virieux, J., 1986, P-SV wave propagation in heterogeneous media: Velocity-stress finite-difference method: Geophysics, **51**, 889–901.

Zeng, Y. Q., J. Q. He, and Q. H. Liu, 2001, The application of the perfectly matched layer in numerical modeling of wave propagation in poroelastic media: Geophysics, **66**, 1258–1266.

Zeng, Y. Q., and Q. H. Liu, 2001a, Acoustic detection of buried objects in 3D fluid-saturated porous media: Numerical modeling: IEEE Transactions on Geoscience and Remote Sensing, **6**, 1165–1173.

———, 2001b, A staggered-grid finite-difference method with perfectly matched layers for poroelastic wave equations: Journal of the Acoustical Society of America, **109**, 2571–2580.

Zhu, X., and G. A. McMechan, 1991, Finite-difference modeling of the seismic response of fluid-saturated, porous, elastic media using Biot theory: Geophysics, **56**, 328–339.